Climate Dynamics
https://doi.org/10.1007/s00382-021-05733-9

# Potential predictability of the MJO during easterly and westerly phases of the QBO

**Chalachew Kindie Mengist**[1,2] · **Kyong-Hwan Seo**[1,2,3] · **Ruiqiang Ding**[4] · **Seok-Woo Son**[5]

Received: 28 September 2020 / Accepted: 10 March 2021

## Abstract

The potential predictability of the Madden–Julian Oscillation (MJO) in boreal winter (November–February) is investigated using observational data for the period of 1979–2016. For various MJO indices, nonlinear local Lyapunov exponents are computed to quantify the MJO predictability under the easterly and westerly phases of the Quasi-Biennial Oscillation (easterly: EQBO and westerly: WQBO). All MJO indices exhibit higher predictability during EQBO winters than during WQBO winters. Excluding strong ENSO years from EQBO and WQBO winters has a limited impact on MJO predictability. The highest potential predictability of 43 days during EQBO winters and 37 days during WQBO winters is found for the MJO index obtained from bandpass-filtered (30–80 days) outgoing longwave radiation and wind data. In contrast, the potential predictability of the MJO from the real-time multivariate MJO index is 21 days during EQBO winters and 13 days during WQBO winters. The longer persistence and less disorganization of the MJO during the EQBO winters lead to the higher predictability for EQBO winters, as compared with that for WQBO winters.

**Keywords** MJO indices · MJO potential predictability · EQBO and WQBO winters · Nonlinear local Lyapunov exponent

## 1 Introduction

The Madden–Julian Oscillation (MJO) is the dominant mode of intraseasonal (30–90 days) variability in the tropics (Madden and Julian 1971, 1972), characterized by eastward propagating tropical circulation and convection anomalies in boreal winter. The MJO affects weather and climate significantly over large areas of the tropics, and its impact stretches out to the mid-latitude and polar regions through Rossby wave trains energized by MJO convection (e.g., Matthews et al. 2004; Seo and Son 2012; Seo and Lee 2017; Lee and Seo 2019). This implies that better MJO prediction could help to improve regional climate forecasting, not only in the tropics but also in the extratropics. However, the MJO predictability remains an open issue. Numerous studies have examined the prediction skill of the MJO. For example, a vector autoregressive (VAR) statistical model for real-time multivariate MJO index (RMMI) developed by Maharaj and Wheeler (2005) shows the MJO prediction skill of ~ 15 days. Recently, the MJO prediction skill of subseasonal-to-seasonal (S2S) reforecast data ranges from 15–36 days (Vitart 2017; Wang et al. 2019a).

Yoo and Son (2016) reported that the Quasi-Biennial Oscillation (QBO) is one of the key factors that determine the MJO amplitude in boreal winter. They showed that the boreal-winter MJO becomes increasingly active for easterly lower-stratospheric zonal winds (EQBO) as opposed to westerly zonal winds (WQBO) (see also Liu et al. 2014; Marshall et al. 2017; Son et al. 2017; Nishimoto and Yoden 2017; Lim et al. 2019). Such a connection between the QBO and MJO also appears in MJO prediction. In the examination of 10 S2S models, Lim et al. (2019) documented that the MJO prediction skill ranges from 13 to 35 days during EQBO winters but only ranges from 10 to 28 days during

✉ Kyong-Hwan Seo
khseo@pusan.ac.kr

[1] BK21 School of Earth and Environmental Systems, Pusan National University, Busan, Republic of Korea

[2] Research Center for Climate Sciences, Pusan National University, Busan, Republic of Korea

[3] Department of Atmospheric Sciences, Pusan National University, Busan, Republic of Korea

[4] State Key Laboratory of Earth Surface Processes and Resource Ecology, Beijing Normal University, Beijing 100875, China

[5] School of Earth and Environmental Sciences, Seoul National University, Seoul, Republic of Korea

WQBO winters. Although not statistically significant (Kim et al. 2019), a higher prediction skill was exhibited by all the S2S models for EQBO winters than for WQBO winters (Lim et al. 2019). It was argued that the strong and well-organized MJO during EQBO winters makes its predictability higher (Marshall et al. 2017; Lim et al. 2019). Wang et al. (2019b) also showed that model forecasted stratosphere QBO has little influence on MJO prediction skill.

Marshall et al. (2017) showed that an improved MJO prediction skill for EQBO winters than for WQBO winters is consistent with the potential predictability of the MJO. Because the predictability of a certain activity is in general approximately equal to its lifetime (Van den Dool and Saha 1990), the potential predictability of the MJO could be as high as 50 days. This implies that the MJO prediction skill of 10–35 days, derived from the state-of-the-art S2S prediction models, underestimates the MJO prediction.

To better understand the QBO–MJO connection and its predictability, the present study revisits the potential predictability of the boreal-winter MJO. Unlike Marshall et al. (2017), which utilized model dependent prediction skill, the potential MJO predictability during the two QBO phases in this study is evaluated from observational data by computing nonlinear local Lyapunov exponent (NLLE; Ding et al. 2010). Ding et al. (2011) reported that the predictability of the boreal-winter MJO is approximately 34 days. However, the potential predictability using NLLE technique during WQBO and EQBO winters remain unknown. In addition, the influence of El Niño-Southern Oscillation (ENSO) for MJO predictability is not analyzed. It is also unclear whether or not the result is sensitive to the choice of the MJO indices (Seo et al. 2009).

By extension of Ding et al. (2011), the NLLE technique is applied to four MJO indices for the following QBO winters: (1) all QBO and neutral-ENSO QBO, (2) EQBO and WQBO, and (3) neutral-ENSO EQBO and neutral-ENSO WQBO. Neutral-ENSO winters are selected to exclude the effect of strong ENSO on the MJO predictability (Song and Wu 2020). The details of the data used in this study and the NLLE technique are described in Sect. 2. The predictability limits of multiple MJO indices are presented in Sect. 3. Finally, Sect. 4 provides the conclusions.

## 2 Data and Methodology

Daily averaged outgoing longwave radiation (OLR) data from the National Oceanic and Atmospheric Administration (NOAA) polar-orbiting series of satellites (Liebmann and Smith 1996) for the period from 1979 to 2016 are used to represent the MJO convection. The OLR data are available at NOAA Earth System Research Laboratory website (https://www.esrl.noaa.gov/psd/data/gridded/data.interp_OLR.html). For the zonal winds at 200 (U200) and 850 hPa (U850), the European Center for Medium-Range Weather Forecasts Re-Analysis data (Dee et al. 2011) are used for the same period. Both OLR and zonal wind data are presented with a horizontal resolution of 2.5° × 2.5°, and only four extended winter months (November, December, January, and February; NDJF) are considered.

In this study, four different MJO indices are considered, as summarized in Table 1. They are the so-called combined MJO index (CMI; Seo et al. 2009), OLR index (OLRI; Seo et al. 2009), OLR-based MJO index (OMI; Kiladis et al. 2014), and RMMI (Wheeler and Hendon 2004). First, anomaly data are obtained by subtracting the time mean and first three harmonics of the annual cycle from OLR, U200, and U850 data over the global tropics (30° S–30° N). The resulting anomalies are normalized by the longitudinally averaged variance (Wheeler and Hendon 2004; Seo et al. 2009) subject to a 30–80-day bandpass Lanczos filter. An empirical orthogonal function (EOF) analysis is then performed to obtain CMI. A similar EOF analysis is conducted with 30–80 day bandpass filtered OLR anomalies to calculate OLRI. The OMI is similar to OLRI, but the filtered OLR anomalies are projected onto the 20–96 day eastward-filtered OLR anomalies (Kiladis et al. 2014). Its long-term data is archived at https://www.esrl.noaa.gov/psd/mjo/mjoindex/. The RMMI is generated by conducting an EOF analysis of latitudinally-averaged OLR, U200, and U850 anomalies (Wheeler and Hendon 2004). Unlike CMI, bandpass filtering is not applied as RMMI is designed to monitor real-time MJO events (Kiladis et al. 2014 and references therein). Note that all the MJO indices are defined by the two leading principal components (PCs). For instance, CMI consists of CMI1

**Table 1** List of MJO time series indices used in this study

| Index | Description |
|---|---|
| CMI | Combined EOF of 30–80 day filtered OLR, U200, and U850 averaged from 30° S to 30° N |
| OLRI | Univariate EOF of 30–80 day filtered OLR data averaged from 30° S to 30° N |
| OMI | Projection of 20–96 day filtered OLR, including all eastward and westward wavenumbers onto the daily spatial EOF patterns of 30–96 day eastward-filtered OLR averaged over 20° S to 20° N |
| RMMI | Real-time combined EOF of normalized OLR, U200, and U850 averaged from 15° S to 15° N |

and CMI2, which correspond to the first- and second-leading PCs (see Wheeler and Hendon 2004 and Kiladis et al. 2014 for more details).

The QBO phase is determined with the zonal-mean zonal wind at 50 hPa averaged over the deep tropics (10° S–10° N). The QBO data, which are directly obtained from the NOAA website (http://www.cpc.ncep.noaa.gov/data/indices/qbo.u50.index), are referred to as the QBO index in this study. If the NDJF-mean QBO index is less or greater than half of its standard deviation, the corresponding winter is defined as an EQBO or WQBO winter (Son et al. 2017; Nishimoto and Yoden 2017). Neutral-ENSO winters are considered when the oceanic Niño Index (https://origin.cpc.ncep.noaa.gov/products/analysis_monitoring/ensostuff/ONI_v5.php) falls between ± 1 °C. Table 2 shows list of QBO years used for evaluating potential predictability of MJO during boreal winter.

According to Ding et al. (2011), the potential predictability of a chaotic system could be estimated by using an NLLE, defined below. First, assume an $n$-dimensional nonlinear dynamical system. For this system, the evolution of a small error $\boldsymbol{\delta} = \left[\delta_1(t), \delta_2(t), \ldots, \delta_n(t)\right]^T$, superimposed on state $\mathbf{x} = \left[x_1(t), x_2(t), \ldots, x_n(t)\right]^{\mathrm{T}}$, is governed by the nonlinear equation:

$$\frac{d}{dt}\boldsymbol{\delta} = \mathbf{J}(\mathbf{x})\boldsymbol{\delta} + \mathbf{G}(\mathbf{x}, \boldsymbol{\delta}) \tag{1}$$

where $\mathbf{x}$ is the state vector at time $t$ and superscript T is the transpose. On the right-hand side, $\mathbf{J}(\mathbf{x})\boldsymbol{\delta}$ represents the tangent linear terms, $\mathbf{J}(\mathbf{x})$ is $\mathrm{n} \times \mathrm{n}$ Jacobian matrix, and $\mathbf{G}(\mathbf{x}, \boldsymbol{\delta})$ represents the high-order nonlinear terms of error $\boldsymbol{\delta}$. Equation (1) could be solved by applying numerical integration along the reference solution $\mathbf{x}$ from $t = t_0$ to $t_0 + \boldsymbol{\tau}$ :

$$\boldsymbol{\delta}\left(t_0 + \boldsymbol{\tau}\right) = \boldsymbol{\eta}\left(\mathbf{x}\left(t_0\right), \boldsymbol{\delta}\left(t_0\right), \boldsymbol{\tau}\right)\boldsymbol{\delta}\left(t_0\right) \tag{2}$$

where $\boldsymbol{\eta}\left(\mathbf{x}\left(t_0\right), \boldsymbol{\delta}\left(t_0\right), \boldsymbol{\tau}\right)$ is the nonlinear propagator, which propagates the initial error forward to the error at $t_0 + \boldsymbol{\tau}$. The NLLE, λ, is then defined as

$$\lambda(\mathbf{x}\left(t_0\right), \boldsymbol{\delta}\left(t_0\right), \boldsymbol{\tau}) = \frac{1}{\tau}\ln\frac{\|\boldsymbol{\delta}\left(t_0 + \boldsymbol{\tau}\right)\|}{\|\boldsymbol{\delta}\left(t_0\right)\|} \tag{3}$$

here, $\lambda(\mathbf{x}\left(t_0\right), \boldsymbol{\delta}\left(t_0\right), \boldsymbol{\tau})$ depends on the initial state $\mathbf{x}\left(t_0\right)$ in phase space, the initial error $\boldsymbol{\delta}\left(t_0\right)$, and time $\boldsymbol{\tau}$. The NLLE differs from an existing local or finite-time Lyapunov exponent defined from linear error dynamics (Ding et al. 2011 and reference therein), which depends solely on the initial state $\mathbf{x}\left(t_0\right)$ and time $\boldsymbol{\tau}$, not on the initial error $\boldsymbol{\delta}\left(t_0\right)$.

The ensemble-mean NLLE over the global attractor of the dynamical system is given by

$$\bar{\lambda}\left(\boldsymbol{\delta}\left(t_0\right), \boldsymbol{\tau}\right) = \int_{\Omega} \lambda(\mathbf{x}\left(t_0\right), \boldsymbol{\delta}\left(t_0\right), \boldsymbol{\tau})d\mathbf{x}$$

$$= \langle\lambda(\mathbf{x}\left(t_0\right), \boldsymbol{\delta}\left(t_0\right), \boldsymbol{\tau})\rangle_N, (N \to \infty) \tag{4}$$

where $\Omega$ represents the domain of the global attractor of the system and $\langle\rangle_N$ denotes the ensemble average of samples of a sufficiently large size $N$ $(N \to \infty)$. The mean relative growth, $\Phi$, of the initial error can be obtained as

$$\bar{\Phi}\left(\boldsymbol{\delta}\left(t_0\right), \boldsymbol{\tau}\right) = \exp\left[\bar{\lambda}\left(\boldsymbol{\delta}\left(t_0\right), \boldsymbol{\tau}\right)\boldsymbol{\tau}\right] \xrightarrow{P} c(N \to \infty) \tag{5}$$

here $\xrightarrow{P}$ denotes the convergence in probability and $c$ is a constant that depends on the converged probability distribution $\mathbf{P}$ of error growth. Once the error growth becomes saturated, prediction becomes meaningless.

In two-dimensional phase space, vector $\mathbf{Z}$ is defined by the first two PCs:

$$\mathbf{Z}(t) = \{\mathrm{PC1}(t),\ \mathrm{PC2}(t)\}. \tag{6}$$

The error of the vector $\mathbf{Z}$ is measured as the absolute error $\sqrt{(\Delta\mathrm{PC1})^2 + (\Delta\mathrm{PC2})^2}$, where ΔPC1 and ΔPC2 are the errors along the PC1 and PC2 axes, respectively. The average error growth of the vector $\mathbf{Z}$ can be obtained from an NLLE approach Ding et al. (2011). Details on how to obtain the average error from the vector $\mathbf{Z}$ are found in supplementary material.

**Table 2** The QBO years used in this study

| QBO | Years |
|---|---|
| All QBO | 1980–2016 |
| Neutral-ENSO QBO | 1980, 1981, 1982, 1984, 1985, 1986, 1988, 1990, 1991, 1993, 1994, 1995, 1996, 1997, 2001, 2002, 2003, 2004, 2005, 2006, 2007, 2009, 2012, 2013, 2014, 2015 |
| EQBO | 1980, 1985, 1990, 1997, 1999, 2002, 2004, 2006, 2008, 2013, 2015 |
| WQBO | 1981, 1983, 1986, 1988, 1989, 1991, 1994, 1996, 1998, 2000, 2003, 2005, 2007, 2009, 2011, 2014, 2016 |
| Neutral-ENSO EQBO | 1980, 1990, 1997, 2002, 2004, 2006, 2013, 2015 |
| Neutral-ENSO WQBO | 1981, 1986, 1988, 1991, 1994, 1996, 2003, 2005, 2007, 2009, 2014 |

The NLLE method is also used to find the predictability limits of the amplitude A($t$) and phase $\alpha(t)$ of the MJO (Lu et al. 2020). The amplitude and phase can be derived from PC1 and PC2:

$$\mathrm{A}(t) = \{\mathrm{PC1}^2(t) + \mathrm{PC2}^2(t)\}^{\frac{1}{2}} \tag{7}$$

$$\alpha(t) = \tan^{-1}\{PC2(t)/PC1(t)\} \tag{8}$$

## 3 Results

As briefly introduced in the previous section, CMI, which consists of CMI1 and CMI2, is derived from filtered OLR, U200, and U850 between 30° S and 30° N during extended winter (NDJF). Figure 1 shows the longitudinal structure of the first two leading EOFs, representing 25.6% and 18.5% of total variance, respectively.

Figure 2a, c, e, and g show the correlation coefficients of PC1 and PC2 during all QBO (red) and neutral-ENSO QBO winters (blue) from CMI, OLRI, OMI, and RMMI. It is evident that the correlations are nearly zero at lag day 0 during all QBO and neutral-ENSO QBO winters. The correlation coefficient is antisymmetric with respect to the lag day for CMI, OLRI, and OMI during all QBO and neutral-ENSO QBO winters. The CMI, OLRI, and OMI show equal lag days (11) with maximum correlation coefficients of 0.75, 0.77, and 0.69, respectively. The RMMI exhibits 7 and 8 lag days with 0.58 and 0.61 correlation coefficients for all QBO and neutral-ENSO QBO winters, respectively. All indices take 8 days to fall below the e-folding of autocorrelation (the time at which the autocorrelation drops to 1/e) for the two winters.

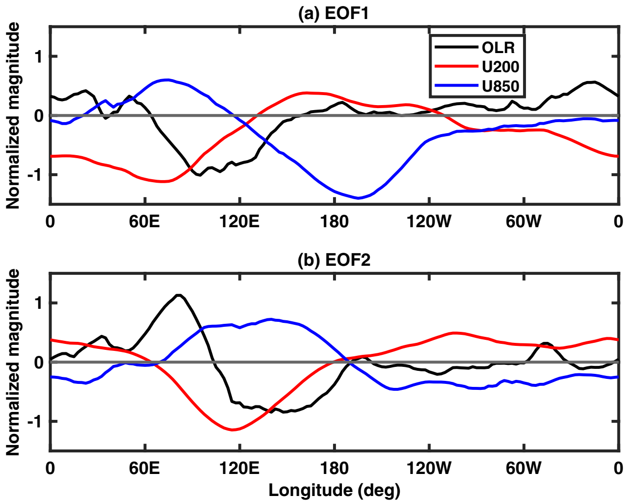

**Fig. 1** EOF analysis from combined data (OLR, U200, and U850) averaged between 30° S and 30° N. **a** EOF1 and **b** EOF2

Figure 2b, d, f and h show the mean error growth of **Z** using CMI, OLRI, OMI, and RMMI during all QBO and neutral-ENSO QBO winters. The mean error growth exhibits an exponential increase and then reaches a saturation level. A rapid increase in the initial error during the first 14 days plays a major role in controlling the mean error growth of MJO over the remaining days. After 14 days, the mean error growth is affected by slowly varying boundary conditions (e.g., external SST forcing; Seo et al. 2007). Once the mean error growth becomes saturated, the prediction becomes meaningless. As such, the potential predictability is defined as the time at which the error reaches 95% of its saturation level (Dalcher and Kalnay 1987). Based on this criterion, the potential predictability of the MJO is 35.5 and 38.5 days for CMI, and 17 and 18 days for RMMI in all QBO and neutral-ENSO QBO winters, respectively. The MJO predictability limits for OLRI and OMI shows similar value of 37 days in all QBO and neutral-ENSO QBO winters. The result from OLRI and OMI shows higher predictability. The lowest MJO predictability limit is found for RMMI. This is due to excessive noise compared with that from bandpass-filtered MJO indices (Ding et al. 2010; Wang et al. 2018). Note also that MJO predictability during all QBO is comparable to that during neutral-ENSO QBO winters, demonstrating that excluding strong ENSO years has a minimal impact on MJO predictability (Yoo and Son 2016; Nishimoto and Yoden 2017).

The correlation coefficients of PC1 and PC2 during EQBO winters and WQBO winters are shown in Fig. 3a, c, e, and g. The non-zero correlations at lag day 0 shown in the figures are due to the lack of orthogonality caused by excluding of non-winter data. The maximum correlation coefficients during EQBO winters for CMI, OLRI, OMI, and RMMI are 0.74, 0.84, 0.75 and, 0.67 respectively. During WQBO winters, they are 0.74, 0.69, 0.61, and 0.57. This result reveals that for most MJO indices except for CMI, the correlation coefficients during EQBO winters are higher than that during WQBO winters. All MJO indices have maximum correlation coefficients at 9–12 lag days during EQBO winters and 7–11 lag days during WQBO winters (Wang et al. 2019b).

The lag correlation coefficients further show that the MJO indices during EQBO winters are more regular and less noisy than those during WQBO winters because the stronger MJO tends to propagate eastward more slowly (Marshall et al. 2017; Lim et al. 2019). The autocorrelation results of the MJO during EQBO winters show more persistent evolution. During EQBO winters, MJO indices take 8–9 days to fall below the e-folding. These values slightly decrease to 7–8 days during WQBO winters.

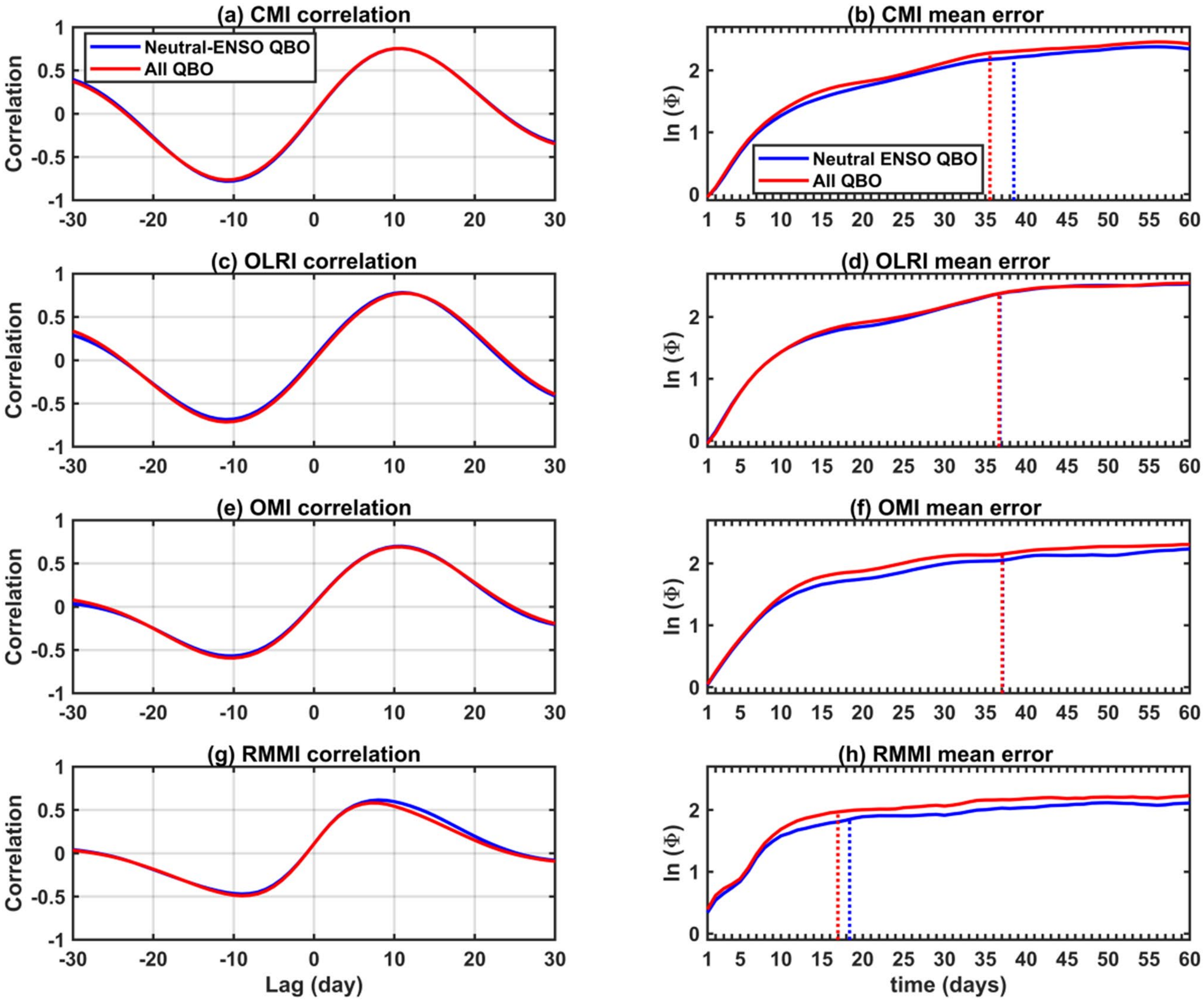

**Fig. 2** Correlation coefficients of PC1 and PC2 during QBO winters (left column) and mean error growth of the vector **Z** from CMI, OLRI, RMMI, and OMI (right column). Positive lag means that convective anomalies move eastward with time. All QBO winters are denoted as red and neutral-ENSO QBO winters are marked in blue

The mean error growth of **Z** during EQBO and WQBO winters are shown in Figs. 3b, d, f and h. The potential predictability of the MJO varies from 40 to 33 days between EQBO and WQBO winters for CMI, from 42 to 36 days for OLRI, from 43.5 to 34 days for OMI, and from 17.5 to 13 days for RMMI. This result is consistent with the recent studies that demonstrated a higher MJO prediction skill for EQBO winters than that for WQBO winters in dynamical model simulations (Marshall et al. 2017; Lim et al. 2019). With the MJO as more persistent and less disorganized during EQBO winters, the prediction skill of the MJO itself is higher during EQBO winters than during WQBO winters. Lim et al. (2019) showed that the MJO amplitude and phase errors are smaller during EQBO winters than WQBO winters. These errors contribute to the MJO prediction skill difference between EQBO and WQBO winters. The predictability limit of amplitude and phase of all QBO, EQBO, and WQBO for OLRI is given in Fig. 4. The result shows that the predictability limit of amplitude of the MJO is smaller than the predictability limit of phase of the MJO (Lu et al. 2020). The predictability limits of amplitude and phase are 26 and 35 days for all QBO; 32 and 37 days for EQBO; 29 and 34 days for WQBO winters, respectively. The predictability limit of phase of the MJO is close to the predictability limit of the MJO itself during all QBO, EQBO, and WQBO winters. The phase of the MJO for CMI, OMI, and RMMI also gives higher predictability than amplitude of the MJO (not shown here). This indicates that the predictability limit of the MJO may be mainly dependent upon the phase of the MJO than amplitude of the MJO. In addition,

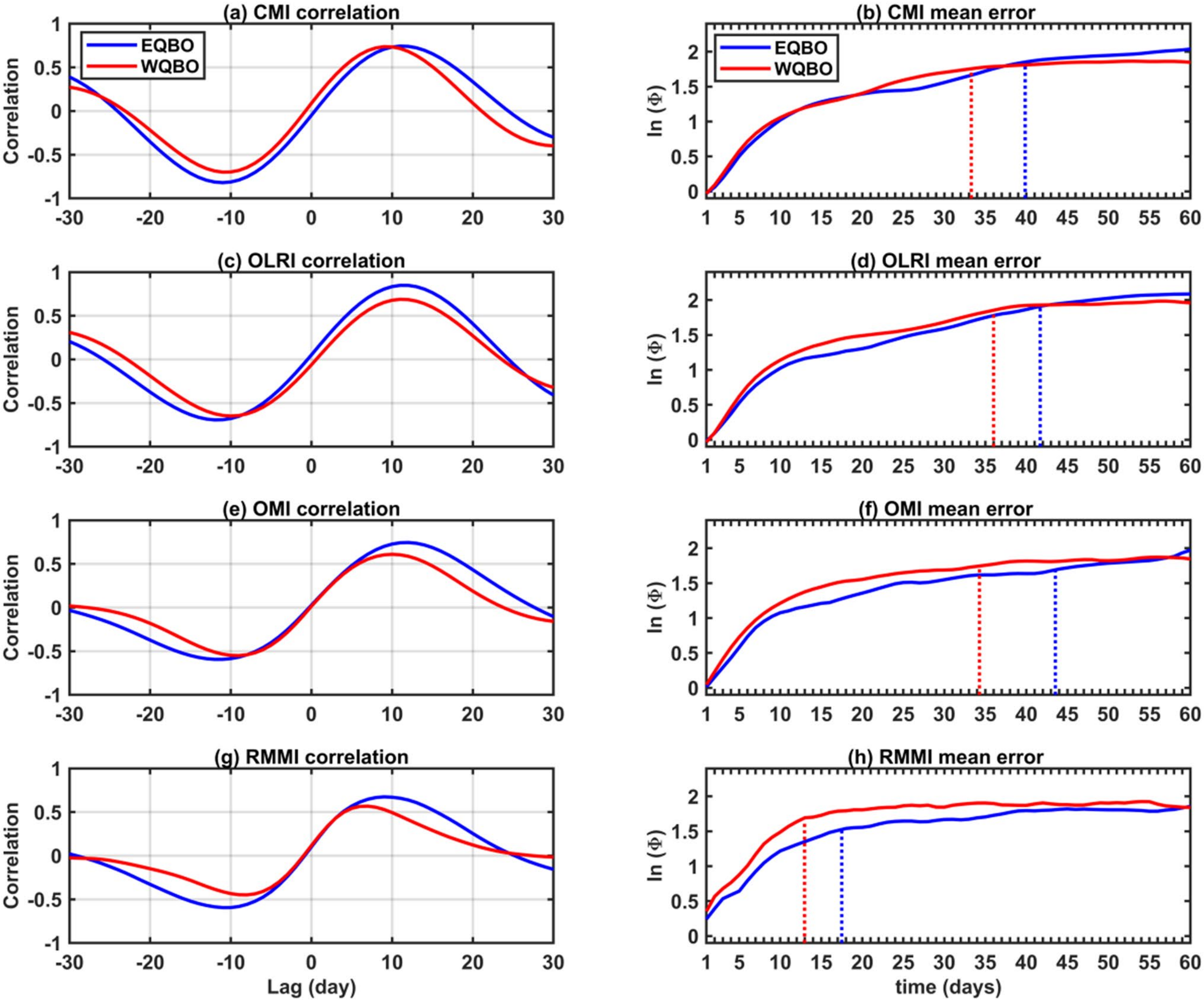

**Fig. 3** Same as Fig. 2 except during EQBO (blue) and WQBO (red) winters

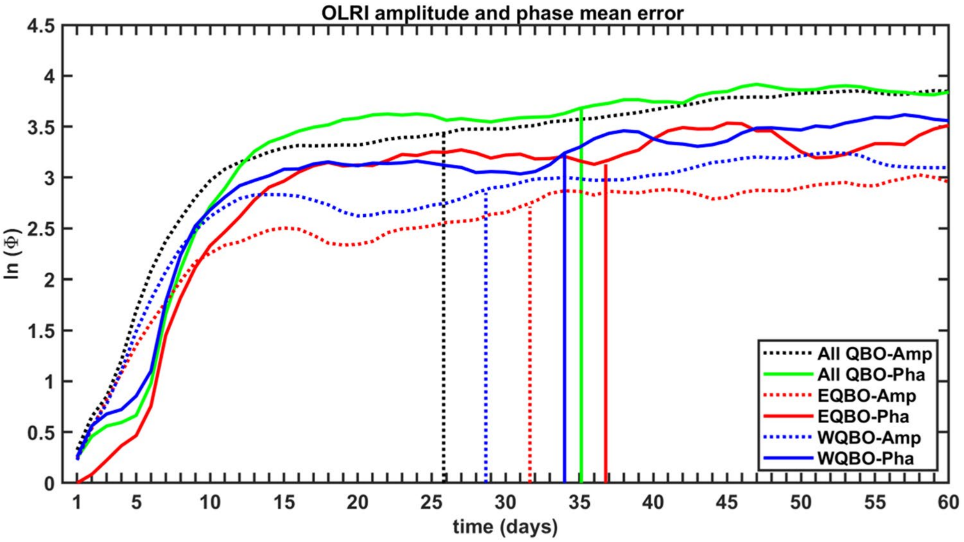

**Fig. 4** Mean error growth of amplitude (dotted line) and phase (solid line) of the MJO from OLRI for all QBO (black and green), EQBO (red), and WQBO (blue) winters

this implies that to improve prediction skill in dynamical model the phase and thus propagation characteristics should be correctly forecasted.

To avoid difficulty in interpreting MJO predictability when strong ENSO events are included, only neutral-ENSO years during EQBO and WQBO winters are further considered. Lag correlations during neutral-ENSO EQBO and neutral-ENSO WQBO winters for CMI, OLRI, OMI, and RMMI have at 9–12 and 7–10 lag days, respectively. The e-folding during neutral-ENSO EQBO winters takes 9 days for CMI, OLRI, and OMI, and 8 days for RMMI. During neutral-ENSO WQBO winters, CMI and OLRI takes 8 days whereas OMI and RMMI takes 7 days. The correlation coefficients and mean error growth of **Z** during neutral-ENSO EQBO and neutral-ENSO WQBO are given in Fig. 5. The maximum correlation coefficients and mean error growth of **Z** during neutral-ENSO EQBO winters are 0.76 and 43 days for CMI, 0.83 and 40 days for OLRI, 0.74 and 42 days for OMI, and 0.70 and 21 days for RMMI, respectively. During neutral-ENSO WQBO winters, CMI, OLRI, OMI, and RMMI have correlation coefficients and mean error growth of 0.76 and 37 days, 0.70 and 38 days, 0.61 and 33 days, and 0.59 and 13 days, respectively. Most importantly, for all indices, the potential predictability of the MJO during EQBO winters is higher than that during WQBO winters. The MJO predictability during EQBO and WQBO did not show significant improvement after removing strong ENSO years. This could be due to insufficient data during neutral-ENSO EQBO (8 years) and neutral-ENSO WQBO (11 years). Li and Ding (2013) pointed out that few data points are not enough to find good local analogues and potential predictability could be underestimated.

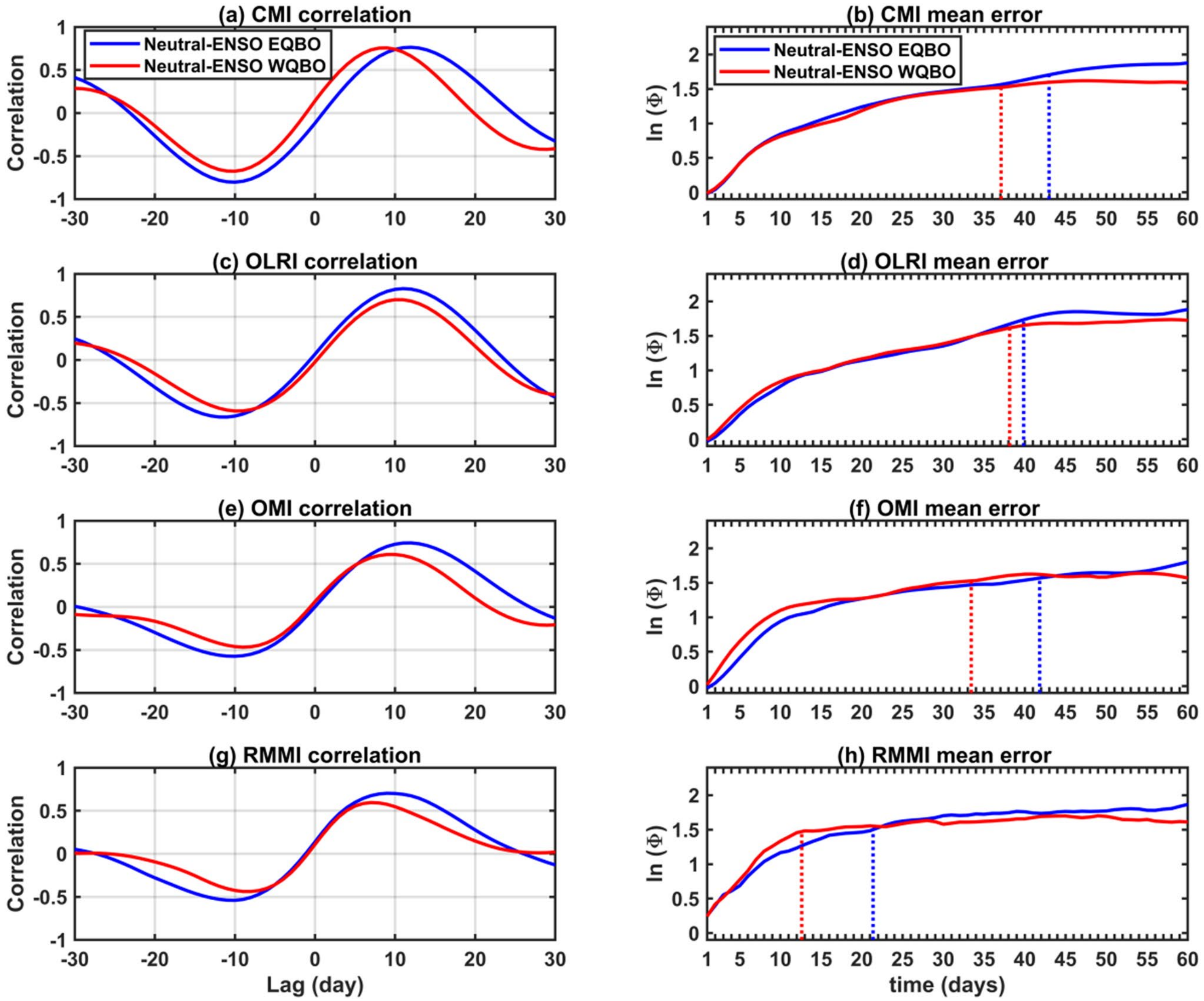

**Fig. 5** Same as Fig. 2 except during neutral-ENSO EQBO (blue) and neutral-ENSO WQBO (red)

The potential predictability, summarized in Table 3, could be influenced by data filtering. The bandpass-filtered data at a given day inevitably contains the information from the past and future days (i.e., a few days before and after a given day). This could increase the predictability limit of the MJO (Seo et al. 2009; Ding et al. 2010). On the other hand, the MJO predictability is insensitive to selection of bandpass filtering days (Lu et al. 2020). According to Ding et al. (2011), the predictability of MJO from filtered noise can be estimated as follows: (1) perform a space–time fast Fourier transform of the two PCs (e.g., CMI1 and CMI2), multiply by their conjugate, and generate random complex numbers that give the same power at each wavenumber and frequency, as in PCs; (2) compute the inverse space–time Fourier transform over the wavenumber–frequency band of the MJO to obtain filtered noise characterized by the same spectrum as the real MJO; (3) apply the NLLE algorithm to find the predictability limit of filtered noise; and (4) repeat the above steps (1–3) 1000 times and obtain 1000 values of potential predictability.

Figure 6 shows the probability distribution of the predictability limit of filtered noise using the above procedures during neutral-ENSO QBO, neutral-ENSO EQBO, and neutral-ENSO WQBO winters. The maximum predictability limit of filtered noise from both CMI and OLRI is approximately 5.5, 6.0, and 6.0 days during neutral-ENSO QBO, neutral-ENSO EQBO, and neutral-ENSO WQBO winters, respectively. The predictability limit of filtered noise for QBO data including ENSO years show 6–8 days (not shown). These values are much smaller than the predictabilities of CMI and OLRI, indicating that the estimated potential predictability of the MJO (Table 3) is mainly driven from the true signal of the data itself, even though the filtered noise increases the predictability to some extent.

**Table 3** MJO predictability limit during all QBO, neutral-ENSO EQBO, and neutral-ENSO WQBO winters

| MJO Index | All QBO | Neutral-ENSO QBO | EQBO | WQBO | Neutral-ENSO EQBO | Neutral-ENSO WQBO |
|---|---|---|---|---|---|---|
| CMI | 35.5 | 38.5 | 40 | 33 | 43 | 37 |
| OLRI | 37 | 37 | 42 | 36 | 40 | 38 |
| OMI | 37 | 37 | 43.5 | 34 | 42 | 33 |
| RMMI | 17 | 18 | 17.5 | 13 | 21 | 13 |

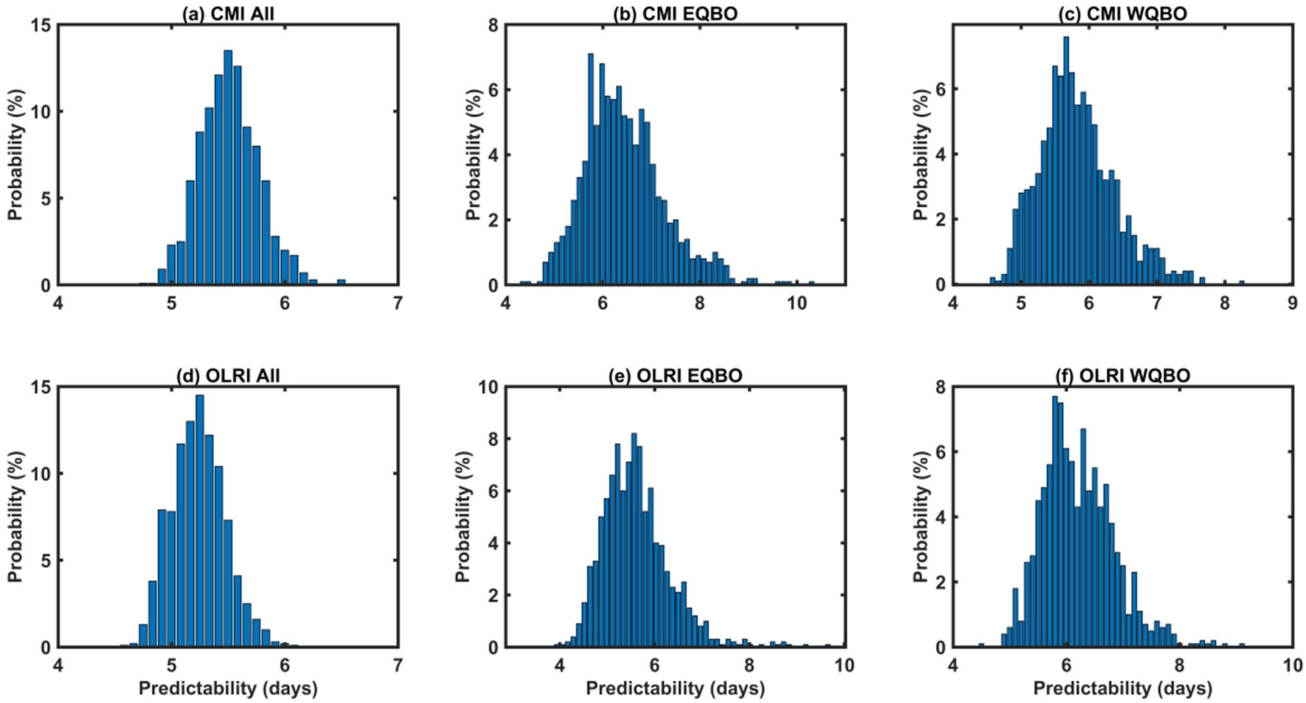

**Fig. 6** Probability distribution of the predictability limits based on filtered noise from CMI (1st row) and OLRI (2nd row)

## 4 Conclusions

We have examined the potential predictability of the MJO in boreal winter (November–February) using observational data for the period of 1979–2016. By applying an NLLE technique to four MJO indices for various QBO winters, the predictability limit is quantified. The potential predictability of the MJO for different indices is summarized as follows:

1. The MJO predictability limit during EQBO winters is higher than that for WQBO winters for all MJO index types, consistent with dynamical model results. This is likely due to the fact that the MJO has longer persistence and is less disorganized during EQBO winters than during WQBO winters.
2. The highest potential predictability of the MJO is obtained from CMI, yielding 43 days during EQBO winters and 37 days during WQBO winters. The RMMI gives the lowest predictability of the MJO during EQBO and WQBO winters, compared with the respective QBO phases from other MJO indices. This difference in the predictability limit of the MJO based on RMMI and CMI reflect the influence of temporal filtering.
3. After ENSO years are excluded for CMI, the predictability limits of the MJO during neutral-ENSO EQBO and neutral-ENSO WQBO are enhanced by 3 and 4 days, respectively. Similarly, RMMI data also shows enhancement of ~ 3 days during neutral-ENSO EQBO (Seo et al. 2009).
4. The predictability from filtered noise is much less than the predictability from MJO data.

It has been shown that the predictability limit of the MJO for RMMI gives 13–21 days. The day-to-day variations of RMMI time series, associated with convectively coupled Kelvin waves and equatorially Rossby waves (Roundy et al. 2009), possibly underestimate the predictability of the MJO. On the other hand, the S2S models (Vitart 2017) show higher prediction skills than the predictability limit for RMMI. The higher prediction skill of the S2S models may have resulted from the smoothness of the MJO indices achieved by the removal of both low-frequency variability through a 120-day running mean and higher-frequency fluctuations through the ensemble averaging. Therefore, a more proper comparison of the prediction skill of the S2S or any other models is against a bandpass-filtering derived index like CMI. Then, the former prediction skill is quite less than the potential predictability limit of CMI. Thus, the authors believe that there is room to improve the prediction skill of the S2S models (Lim et al. 2019; Vitart 2017).

The results in this report could be used as a benchmark for existing numerical and statistical models to improve the prediction skill of the MJO during QBO. The predictability limit of phase of the MJO is closer to the predictability limit of the MJO itself than the predictability limit of amplitude of the MJO does. Therefore, to improve prediction skill of the MJO in dynamical models, proper simulation of phase and thus propagation characteristics needs to be achieved.

One caveat of this study is sample size. Because of limited observation data, the MJO predictability during ENSO winters are not conducted. Using numerical model that simulates both the MJO and ENSO realistically, the effect of ENSO on the MJO predictability under EQBO and WQBO winters could be estimated.

**Supplementary Information** The online version contains supplementary material available at https://doi.org/10.1007/s00382-021-05733-9.

**Acknowledgements** This work was supported by the National Research Foundation of Korea (NRF) grant funded by the Korea government (MSIP) (No. NRF-2020R1A2C2009414) and Korea Meteorological Administration (KMA) Research and Development Program under Grant KMI 2018–01012.

## References

Dalcher A, Kalnay E (1987) Error growth and predictability in operational ECMWF forecasts. Tellus A 39A(5):474–491

Dee et al (2011) The ERA-interim reanalysis: configuration and performance of the data assimilation system. Quart J Roy Met Soc 137:535–597

Ding RQ, Li JP, Seo KH (2010) Predictability of the Madden–Julian oscillation estimated using observational data. Mon Weather Rev 138:1004–1013. https://doi.org/10.1175/2009MWR3082.1

Ding RQ, Li JP, Seo KH (2011) Estimate of the predictability of boreal summer and winter intraseasonal oscillations from observations. Mon Weather Rev 139:2421–2438. https://doi.org/10.1175/2011MWR3571.1

Kiladis GN, Dias J, Straub KH, Wheeler MC, Tulich SN, Kikuchi K, Weickmann KM, Ventrice MJ (2014) A comparison of OLR and circulation-based indices for tracking the MJO. Mon Weather Rev 142:1697–1715. https://doi.org/10.1175/MWR-D-13-00301.1

Kim H, Richter JH, Martin Z (2019) Insignificant QBO-MJO prediction skill relationship in the SubX and S2S subseasonal reforecasts. J Geophys Res Atmos 124:12655–12666. https://doi.org/10.1029/2019JD031416

Lee HJ, Seo KH (2019) Impact of the Madden-Julian oscillation on Antarctic sea ice and its dynamical mechanism. Sci Rep 9:1–10. https://doi.org/10.1038/s41598-019-47150-3

Li J, Ding RQ (2013) Temporal–spatial distribution of the predictability limit of monthly sea surface temperature in the global oceans. Int J Climatol 33:1936–1947. https://doi.org/10.1002/joc.3562

Liebmann B, Smith CA (1996) Description of a complete (interpolated) outgoing longwave radiation dataset. Bull Am Meteorol Soc 77(6):1275–1277

Lim Y, Son SW, Marshall AG, Hendon HH, Seo KH (2019) Influence of the QBO on MJO prediction skill in the subseasonal-to-seasonal prediction models. Clim Dyn 53:1681–1695. https://doi.org/10.1007/s00382-019-04719-y

Liu C, Tian B, Li KF, Manney GL, Livesey NJ, Yung YL, Waliser DE (2014) Northern Hemisphere mid-winter vortex-displacement and vortex-split stratospheric sudden warmings: influence of the madden-julian oscillation and quasi-biennial oscillation. J Geophys Res Atmos 119(12):12599–12620. https://doi.org/10.1002/2014JD021876

Lu D, Ding RQ, Li J (2020) The predictability limit of the amplitude and phase of the Madden-Julian oscillation. Atmos Sci Lett 21:e968. https://doi.org/10.1002/asl.968

Madden RA, Julian PR (1971) Detection of a 40–50 day oscillation in the zonal wind in the tropical Pacific. J Atmos Sci 28:702–708. https://doi.org/10.1175/1520-0469(1971)028%3c0702:DOADOI%3e2.0.CO;2

Madden RA, Julian PR (1972) Description of global-scale circulation cells in the tropics with a 40–50 day period. J Atmos Sci 29(6):1109–1123. https://doi.org/10.1175/1520-0469(1972)029%3c1109:DOGSCC%3e2.0.CO;2

Maharaj EA, Wheeler MC (2005) Forecasting an index of the madden-oscillation. Int J Climatol 25(12):1611–1618

Marshall AG, Hendon HH, Son SW, Lim Y (2017) Impact of the quasi-biennial oscillation on predictability of the Madden–Julian oscillation. Clim Dyn 49:1365–1377. https://doi.org/10.1007/s00382-016-3392-0

Matthews AJ, Hoskins BJ, Masutani M (2004) The global response to tropical heating in the Madden–Julian oscillation during Northern winter. Q J R Meteor Soc 130:1991–2011. https://doi.org/10.1256/qj.02.123

Nishimoto E, Yoden S (2017) Influence of the stratospheric quasi-biennial oscillation on the Madden–Julian oscillation during austral summer. J Atmos Sci 74:1105–1125. https://doi.org/10.1175/JAS-D-16-0205.1

Roundy PE, Schreck CJ III, Janiga MA (2009) Contributions of convectively coupled equatorial Rossby waves and Kelvin waves to the real-time multivariate MJO indices. Mon Weather Rev 137(1):469–478

Seo KH, Lee HJ (2017) Mechanisms for a PNA-like teleconnection pattern in response to the MJO. J Atmos Sci 74:1767–1781. https://doi.org/10.1175/JAS-D-16-0343.1

Seo KH, Son SW (2012) The global atmospheric circulation response to tropical diabatic heating associated with the Madden-Julian oscillation during northern winter. J Atmos Sci 69:79–96. https://doi.org/10.1175/2011JAS3686.1

Seo KH, Schemm JKE, Wang W, Kumar A (2007) The boreal summer intraseasonal oscillation simulated in the NCEP Climate Forecast System (CFS): the effect of sea surface temperature. Mon Weather Rev 135:1807–1827. https://doi.org/10.1175/MWR3369.1

Seo KH, Wang W, Gottschalck J, Zhang Q, Schemm JKE, Higgins WR, Kumar A (2009) Evaluation of MJO forecast skill from several statistical and dynamical forecast models. J Clim 22:2372–2388. https://doi.org/10.1175/2008JCLI2421.1

Son SW, Lim Y, Yoo C, Hendon HH, Kim J (2017) Stratospheric control of Madden–Julian oscillation. J Clim 30:1909–1922. https://doi.org/10.1175/JCLI-D-16-0620.1

Song L, Wu R (2020) Modulation of the QBO on the MJO-related surface air temperature anomalies over Eurasia during boreal winter. Clim Dyn 54:2419–2431. https://doi.org/10.1007/s00382-020-05122-8

Van den Dool HM, Saha S (1990) Frequency dependence in forecast skill. Mon weather Rev 118:128–137. https://doi.org/10.1175/1520-0493(1990)118%3c0128:FDIFS%3e2.0.CO;2

Vitart F (2017) Madden–Julian oscillation prediction and teleconnections in the S2S database. Q J R Meteor Soc 143:2210–2220. https://doi.org/10.1002/qj.3079

Wang S, Ma D, Sobel AH, Tippett MK (2018) Propagation characteristics of BSISO indices. Geophys Res Lett 45:9934–9943. https://doi.org/10.1029/2018GL078321

Wang S, Sobel AH, Tippett MK, Vitart F (2019a) Prediction and predictability of tropical intraseasonal convection: seasonal dependence and the Maritime Continent prediction barrier. Clim Dyn 52:6015–6031. https://doi.org/10.1007/s00382-018-4492-9

Wang S, Tippett MK, Sobel AH, Martin ZK, Vitart F (2019b) Impact of the QBO on prediction and predictability of the MJO convection. J Geophys Res Atmos 124:1766–11782. https://doi.org/10.1029/2019JD030575

Wheeler M, Hendon HH (2004) An all-season real-time multivariate MJO index: development of an index for monitoring and prediction. Mon Weather Rev 132:1917–1932. https://doi.org/10.1175/1520-0493(2004)132%3c1917:AARMMI%3e2.0.CO;2

Yoo C, Son SW (2016) Modulation of the boreal wintertime Madden–Julian oscillation by the stratospheric quasi-biennial oscillation. Geophys Res Lett 43:1392–1398. https://doi.org/10.1002/2016GL067762